In-situ Investigations on Gold Nanoparticles Stabilization Mechanisms in Biological Environments Containing HSA

Pushing the boundaries of chemistry? It takes #HumanChemistry

Make your curiosity and talent as a chemist matter to the world with a specialty chemicals leader. Together, we combine cutting-edge science with engineering expertise to create solutions that answer real-world problems. Find out how our approach to technology creates more opportunities for growth, and see what chemistry can do for you at:

evonik.com/career

EVONIK
Leading Beyond Chemistry

ADVANCED FUNCTIONAL MATERIALS
www.afm-journal.de

In-situ Investigations on Gold Nanoparticles Stabilization Mechanisms in Biological Environments Containing HSA

*Neda Iranpour Anaraki, Marianne Liebi, Quy Ong, Clément Blanchet, Anjani K. Maurya, Francesco Stellacci, Stefan Salentinig, Peter Wick, and Antonia Neels**

Nanoparticles (NPs) developments advance innovative biomedical applications. However, complex interactions and the low colloidal stability of NPs in biological media restrict their widespread utilization. The influence of NPs properties on the colloidal stability for gold NPs with 5 and 40 nm in diameter with two surface modifications, methoxy-polyethylene glycol-sulfhydryl (PEG) and citrate, in NaCl and human serum albumin (HSA) protein solution, is investigated. This study is based on small-angle X-ray scattering (SAXS) methods allowing the in-situ monitoring of interactions in physiological conditions. The PEG coating provides high colloidal stability for NPs of both sizes. For 5 nm NPs in NaCl solution, a stable 3D self-assembled body-centered cubic (BCC) arrangement is detected with an interparticle distance of 20.7 ± 0.1 nm. In protein solution, this distance increases to 21.9 ± 0.1 nm by protein penetration inside the ordered structure. For citrate-capped NPs, a different mechanism is observed. The protein particles attach to the NPs surfaces, and an appropriate concentration of proteins results in a stable suspension. Cryogenic transmission electron microscopy (Cryo-TEM), UV–visible spectroscopy, and dynamic light scattering (DLS) support the SAXS results. The findings will pave the way to design and synthesize NPs with controlled behaviors in biomedical applications.

1. Introduction

The application of NPs expand in various domains of human life including energy, electronics, and medicine due to their remarkable properties owing to their large surface area. However, their unpredictable behavior in biological environments restricts their evolution in biological and biomedical applications. Transferring NPs to a complex biological media may result in NPs aggregation, NPs dissolution, or layer (protein, NPs oxidation) formation on NPs surfaces. These changes drastically affect NPs functionality and behavior in biological media such as cellular uptake.[1]

Broad knowledge about NPs design, stabilization, interactions, and underlying models is developed in the last decades.[2] However, the information about dynamic mechanisms governing NPs interactions with other molecules, their probable behavior, and structural changes in different physicochemical and biological conditions is still limited.[3] Furthermore, NPs size and surface properties, such as charge and polarity play a crucial role in these processes, particularly for very small NPs within the size range of proteins.[4] Therefore, accurate in-situ characterizations on realistic time scales and initial environments will provide essential data for understanding the early stage of NPs interactions with competing particles and identifying the driving forces in NPs aggregation and corona formation. This information helps to predetermine NPs behaviors and resultantly to steer their behavior in the biological environment.[5]

Gold NPs are important in various imaging methods and medical therapies because of their unique electrical, optical,

N. Iranpour Anaraki, M. Liebi, A. K. Maurya, A. Neels
Center for X-ray Analytics
Empa
Swiss Federal Laboratories for Materials Science and Technology
Lerchenfeldstrasse 5, St. Gallen 9014, Switzerland
E-mail: antonia.neels@empa.ch

N. Iranpour Anaraki, P. Wick
Laboratory of Particles-Biology Interactions
Empa
Swiss Federal Laboratories for Materials Science and Technology
Lerchenfeldstrasse 5, St. Gallen 9014, Switzerland

The ORCID identification number(s) for the author(s) of this article can be found under https://doi.org/10.1002/adfm.202110253.

DOI: 10.1002/adfm.202110253

N. Iranpour Anaraki, S. Salentinig, A. Neels
Department of Chemistry
University of Fribourg
Chemin du Musée 9, Fribourg 1700, Switzerland

M. Liebi
Department of Physics
Chalmers University of Technology
Gothenburg 41296, Sweden

Q. Ong, F. Stellacci
Institute of Materials
Ecole Polytechnique Fédérale de Lausanne (EPFL)
Lausanne 1015, Switzerland

C. Blanchet
European Molecular Biology Laboratory
Hamburg Outstation
Notkestrasse 85, 22603 Hamburg, Germany

A. K. Maurya
Stanford Synchrotron Radiation Lightsource
SLAC National Accelerator Laboratory
Menlo Park, CA 94025, USA

thermal, and chemical properties and their biocompatibility with human cells. Therefore, gold NPs present an excellent opportunity to serve as a model system. Protein adsorption and NPs aggregation are two main processes that gold NPs face in biological media. The available strategies to achieve more stable NPs in complex biological environments are electrostatic repulsion or steric stabilisation by adding a physical barrier on the NPs surface such as attaching polyethylene glycol (PEG).[6]

Higher ionic strength (IS) in biological media compare to the initial IS of NPs suspensions screens the NPs surface charge and results in aggregation of charge stabilized systems. The Derjaguin–Landau–Verwey–Overbeek (DLVO) theory assumes that repulsive Van-der-Waals forces and attractive electrostatic double-layer forces are independent and therefore can be superimposed or added at each interacting distance for two particles. The total interaction potential has a maximum, representing the aggregation energy barrier, determining the colloidal stability of the particles. This maximum is the energy that two NPs must overcome during the collision to stick to each other and get aggregated. By increasing the IS, this energy barrier decreases, and NPs aggregate faster.[4a,7] Therefore, the electrostatic stabilization method is mostly compromised in NPs biomedical and biological applications due to the higher IS in biological environments than the initial IS of NPs suspensions. NPs functionalization with various polymers provides not only a physical barrier to prevent NPs collisions, but also due to the hydrophilic nature of polymers, the short-range repulsive hydration forces induce an extra stabilization.[2b]

Due to their composition with hydrophobic and hydrophilic amino acids, proteins are mostly amphipathic, i.e., they have both polar and nonpolar parts, and can interact with almost any surface, including NPs.[8] Proteins adsorb on the NPs surface via several forces, namely electrostatic, Van-der-Waals, and hydrophobic forces, and form the protein corona (PC) around NPs upon entering biological media. Different theories regarding the formation of PC have been reported. The Vroman effect states that in a system with various proteins, first the proteins with higher mobility adsorb on the NPs surface, and with time, more stable and less mobile proteins replace them.[4b] Another theory by Hirish et al. considers a transient complex that is a multilayered protein aggregate on the NPs surface, and the dynamic exchange occurs via this layer.[9] The dynamic density functional theory (DDFT) combines steric and electrostatic interactions. This theory considers adsorption energy, bulk density, and protein charge in addition to the classical diffusion-based Vroman effect.[10]

NPs composition, size, shape, crystallinity, surface properties, and physicochemical properties of the respective media play a role in PC composition.[4a,11] The PC formation causes two main issues: the possible change in NPs colloidal stability and creating a new biological identity for the NPs. Both of these phenomena drastically affect the NPs functionality and their useful lifetime.[2b]

The PC can be investigated directly by analyzing the adsorbed proteins on the NPs surface with, for instance, mass spectrometry and circular dichroism methods, or indirectly, by measuring the changes in NPs properties due to the PC, such as their size. Only a few techniques are label-free in both cases and allow in-situ studies on the PC without removing unbound proteins from the probed volume before the measurements to keep the equilibrium state, which is essential for biomedical applications.[11a,12]

However, if the NPs reach the same size as the interacting proteins, the current models estimating the NPs colloidal behavior are insufficient and have to be refined. Therefore, we performed real-time experiments in realistic NPs environments to study the influence of gold NPs size, their surface modifications, and protein concentration on NPs-Protein interactions and how these complex interactions affect the NPs colloidal stability. SAXS is used as the primary characterization method. SAXS allows determining NPs size, size distribution, shape, and probable interactions. It provides the statistical information averaged over a macroscopic sample volume.[13] The unique strength of SAXS, which is vital for NPs research, is to study colloidal systems in real-time, label-free, and under their realistic, native environments.[14] Before, this method has been used to study NP-NP[15] interactions or NPs-Protein[16] interactions to describe the adsorption of protein molecules on NP surface. In this study, we describe and focus on NP-NP interactions and the changes in their colloidal stability in biological media.

UV–visible spectroscopy, cryo-TEM, DLS, and zeta potential measurements are applied as complementary methods for studying our NPs systems.

2. Experimental Section

2.1. Gold NPs

BioPure gold Nanospheres, monodispersed and unaggregated colloids, were purchased from nanoComposix (San Diego, CA, USA) and used without further purification. The initial concentration was 1 mg mL^{-1}.

Spherical NPs with two sizes, 5 and 40 nm in diameter, with two different surface modifications, citrate, and PEG 5 kDa, were used to study the effect of NPs size and surface modification on NPs behavior in the biological environment. The NPs with 5 nm in diameter had a comparable diameter with HSA particles.[17] The NPs samples were diluted to desired concentrations just before each experiment with deionized (DI) water, and measurements were done 10 min after sample preparation.

2.2. Human Serum Albumin

HSA is the most abundant protein in human blood plasma, with a concentration of 35–50 mg mL^{-1}. HSA is robust concerning pH and temperature changes.[17,18] The HSA solution from CSL Behring (Pennsylvania, USA), 20% w/v, was used. It is a medical product, and the protein is highly stable in this solution and does not show any aggregation. The protein concentration was adjusted with a NaCl solution of 0.9% w/v and prepared freshly for each experiment.

HSA protein solutions were prepared based on the number of NPs in the sample. Despite the mass concentration being equal for all NPs samples (0.033 mg mL^{-1}), their particle concentrations were significantly different due to the different sizes. Two different protein numbers per NP (Pr/NP) were considered: 100, 1000, and a solution with a high protein

Table 1. HSA concentration for each NPs sample in Pr/NP ratio: 100 and 1000 and Pr/NP ratio for the sample in 4 mg mL^{-1} HSA protein solution.

Samples	Number of NPs per mL in concentration 0.033 mg mL^{-1}	Protein concentration for Pr/NP:100 mg mL^{-1}	Protein concentration for Pr/NP:1000 mg mL^{-1}	Pr/NP ratio in samples with 4 mg mL^{-1} HSA concentration
40 nm PEG	5×10^{10}	0.00056	0.00566	706 614
40 nm citrate	5×10^{10}	0.00054	0.00544	734 056
5 nm PEG	3.4×10^{13}	0.337	3.374	1078
5 nm citrate	2.6×10^{13}	0.285	2.853	1402

concentration, 4 mg mL^{-1}, as used in biological solutions corresponding to >700 000 Pr/NP for the 40 nm NPs, and >1000 Pr/NP for the 5 nm NPs.[19] **Table 1** shows the protein concentration and the Pr/NP ratio for each sample. The number of NPs/mL was calculated based on the information provided by the company for NPs number concentration.

2.3. NaCl Solution

Sodium chloride (≥99.5%) (NaCl) was purchased from Sigma Aldrich and used without further purification. NaCl solution of 0.9% w/v was used to dilute the initial HSA solutions. All experiments were carried out at room temperature.

2.4. Small-Angle X-Ray Scattering

SAXS data were collected on the P12 beamline of EMBL at the PETRA III storage ring (DESY, Hamburg).[20] The X-ray wavelength of 0.124 nm (photon energy $E = 10$ keV) was used for the measurement. An EIGER 4M detector (Dectris) and a sample to detector distance of 3 m (calibrated using AgBeh) were used to collect photons scattered between magnitudes of the scattering vector, q, of 0.025 and 2.9 nm^{-1}, ($q = 4(\pi/\lambda)(\sin\theta/2)$), where θ is the scattering angle and λ is X-ray wavelength. In the discussion section, this q-range was selected based on the NP sizes for further analysis. (a smaller q-range was selected for large NP whose SAXS signal was mainly in the very small angle region).

The NPs sample solutions were loaded into quartz capillaries with a diameter of 1.5 mm (Hilgenberg GmbH, Germany) in a sample holder in front of the incident X-ray beam (Figure S1, Supporting Information). Three different points from up to the bottom of the capillary were selected for measurements. For each measurement, 40 successive frames of 100 ms were collected to check the radiation damage for NPs and protein samples. The damage sample data were excluded from the data directly, and afterward, the 2D SAXS images were radially averaged and normalized to the transmitted beam intensity using the beamline data pipeline.[21] The scattering of water and NaCl solution was subtracted from the sample scattering for background correction.

2.5. SAXS Data Analysis

The SASfit software was used for data analysis and fitting the SAXS data.[22]

The applied model for scattering of spherical particles was

$$I(q,r,\Delta\eta) = \frac{4}{3}\pi r^3 \Delta\eta 3 \frac{\sin qr - qr\cos qr}{(qr)^3} \tag{1}$$

where r is the sphere radius and $\Delta\eta$ is the scattering length density difference between particle and matrix.

The distribution can be considered for different parameters that we used Gaussian distribution for particle radius.

$$\text{Gaussian}(x) = \frac{N}{c} e^{\left\{-\frac{1}{2}\left(\frac{x-x_0}{s}\right)^2\right\}} \tag{2}$$

where N is the concentration parameter, s, width parameter, and x_0 is the mean radius parameter.

For particles interactions together, two structure factor models were considered. The aggregated samples were fitted with the sticky-hard sphere model that is Baxter's model of the adhesive hard sphere. The interaction potential $U(r)$ is

$$\frac{U(r)}{k_B T} = \begin{cases} \infty & \text{for} \quad 0 < r < R_0 \\ \ln\dfrac{12\tau\Delta}{\sigma+\Delta} & \text{for} \quad R_0 < r < R_0+\Delta \\ 0 & \text{for} \quad r > R_0+\Delta \end{cases} \tag{3}$$

where R_0 is the particle radius, Δ is the interparticle distance, and τ is the stickiness parameter. If $\tau > 0$, the potential is attractive, and if $\tau < 0$, the potential is repulsive.

The structure factor is

$$S(q, R_{HS}) = \frac{1}{1 - C(q, R_{HS})} \tag{4}$$

where $C(q, R_{Hs}) = \frac{2\eta\lambda}{k}\sin(k) - 2\left(\frac{\eta\lambda}{k}\right)^2 (1-\cos(k)) - \{\alpha k^3(\sin(k) - k\cos(k)) + \beta k^2(2k\sin(k) - (k^2-2)\cos k - 2) + \frac{\eta\alpha}{2}((4k^3-24k)\sin(k) - (k^4 - 12k^2 + 24)\cos(k) + 24)\}$

Here $k = 2qR_{HS}$ and

$$\alpha = \frac{(1+2\eta-\mu)^2}{(1-\eta)^4} \tag{5}$$

$$\beta = -\frac{3\eta(2+\eta)^2 - 2\mu(1+7\eta+\eta^2) + \mu^2(2+\eta)}{2(1-\eta)^4} \tag{6}$$

where $\eta = f_p\left(\frac{2R_{HS}+\Delta}{2R_{HS}}\right)$, $\varepsilon = \tau + \frac{\eta}{1-\eta}$, $\gamma = f_p\frac{1+\eta/2}{3(1-\eta)^2}$, $\lambda = \frac{6}{\eta}(\varepsilon - \sqrt{\varepsilon^2-\gamma})$ and $\mu = \lambda\eta(1-\eta)$. In the hard sphere model R_{HS} is hard sphere repulsion radius, τ is stickiness parameter, and f_p is the particle volume fraction.

For large structures going beyond the resolution limit of the SAXS experiment setup, a power-law scattering was added similar to the Porod scattering of big particles to account for the low-q upturn. The final can be described as

$$I(q) = I(q, r, \Delta\eta)S(q, R_{HS}, f_p, \tau) + C_p/q^p \tag{7}$$

C_p and p describes the prefactor and exponent of the power-law, respectively.

Another structure factor model, the BCC-iso-Gaussian was used for ordered PEGylated NPs. The structure factor for randomly oriented domains of the ordered particle can be written as

$$S(q) = (Z_0(q) - 1)g(q) + 1 \tag{8}$$

$Z_0(q)$ is the lattice factor get an ideal undistorted lattice and $g(q)$ is the Debye–Waller factor. The lattice factor expressed with Miller indices is as

$$Z_0(q) = \frac{(2\pi)^{d-1}}{n v_d \Omega_d q^{d-1}} \sum_{\{hkl\}} m_{hkl} f_{hkl}^2 L_{hkl}(q - q_{hkl}) \tag{9}$$

where n is the number of particles per unit cell, f_{hkl} is the symmetry factor taking into account extinction rules, v_d is the volume, Ω_d is the d-dimensional solid angle, $L_{hkl}(q - q_{hkl})$ is a normalized peak-shape function, and m_{hkl} is the multiplicity. If the sum was done over all reflections $\{hkl\}$, one automatically accounted for multiplicity but one the costs for summing over all combinations of $\{hkl\}$. For the normalized peak shape function $L_{hkl}(x)$ the Gaussian peak shape was chosen.

$$L_{hkl}(x) = \frac{2}{\pi\delta}\exp\left(-4\frac{x^2}{\pi\delta}\right) \tag{10}$$

It should be noted that the reported uncertainties for different parameters are only the uncertainty contributions from the fitting. These uncertainties were used for determination of the combined standard uncertainties from all input quantities.[22]

All the peak positions were calculated using the peak analyzer tool or the Gaussian peak fitting function of the Origin 2020b (OriginLab Corporation, Northampton, MA, USA).

For the indexing of the data and visualizing the diffraction peaks, the HighScorePlus software[23] was used. The molecular BCC drawing, including the respective diffraction planes, was created using Mercury.[24]

2.6. UV–Visible Spectroscopy

UV–visible absorption spectroscopy with a simple experimental setup is a standard and one of the most widespread analyses for gold NPs characterization. Based on the Mie theory, the surface plasmon resonance (SPR) band's intensity and wavelength were related to the size, shape, composition, colloidal stability, and dielectric constant of the surrounding media.[3a,25] In addition, the concentration and the dispersity of the gold NPs can be determined by the peak intensity and the FWHM (Full-Width at Half Maximum), respectively. UV–vis spectra were collected on a Laurier Cary-50 UV–vis spectrophotometer with the wavelength range from 400 to 850 nm using a 96 well plate.

2.7. Dynamic Light Scattering

The fresh NPs suspensions with desired concentration were prepared directly before the measurements. A Zetasizer Nano ZS90 Malvern instrument operating with a He–Ne laser at a wavelength of 633 nm was used to measure the NPs zeta potential and the apparent hydrodynamic diameter (d_h) at 25 °C and pH 7. The salt molarity in water solution is zero since DI water is used for all sample preparations, and it is 0.15 mol L^{-1} in NaCl solution. The scattering angle is 90°. The water refractive index for these measurements was considered with 1.33.[26] The Smoluchowski approximation was applied in the zeta potential determination. Measurements were done in triplicates and the average results were used.

2.8. Cryogenic Transmission Electron Microscopy

2D and tilt-series cryo-TEM images were recorded in a Tecnai F20 microscope (Thermofisher), operated at 200 kV, and equipped with a cryo holder Gatan 626 (Gatan Inc.). The drift-corrected tilt series were acquired automatically from –60° to +60° with an angular increment of 2° at an electron dose of ≈40 $e^-/Å^2$ by a Falcon III camera (Thermofisher) with 4096 × 4096 pixels. NPs colloid samples were applied onto a holey-film grid. Excess dispersion was blotted away from one side of the grid using a Whatman ashless grade-41 filter paper. The vitrification was done by liquid ethane in a home-made plunge freezer. Quantifoil R1.3/1.2 (EMS) grids were mainly used, in addition to larceny carbon films (200 mesh, EMS) and gold quantifoils (R2/2, 200 mesh, EMS). The imaging was performed at the magnification of 50 000×, with a defocus range from –3 to –5 µm. The tilt series were binned (2×) and aligned using cross-correlations by Inspect 3D (Thermofisher). Tomograms were reconstructed by SIRT from Inspect 3D using 24 iterations. The tomograms were analyzed with ImageJ (NIH).

3. Results and Discussions

The effect of gold NPs size and surface modification on their colloidal stability in various IS and protein concentrations are investigated. The initial size of the NPs in the stock solution (Figure S2, Supporting Information) was measured by SAXS, and the results are compliant with the information giving by the company providing the NPs for our study.

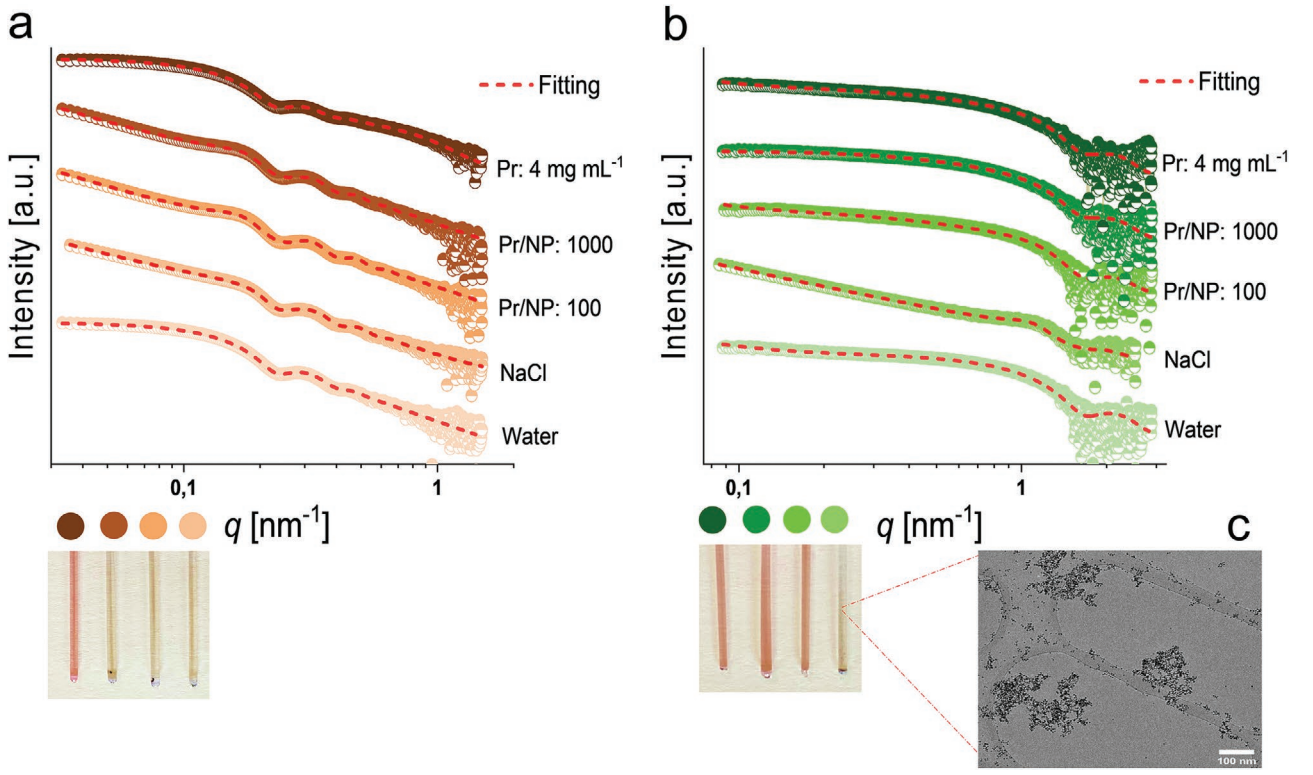

Figure 1. Experimental SAXS patterns and corresponding model-based fits for citrate-capped NPs in different environments: a) 40 nm citrate NPs, b) 5 nm citrate NPs. Below the graphs, the capillaries which were used in the experiments are shown. The pink color indicates stable gold NPs and colorless solutions contain aggregated and precipitated NPs. c) Cryo-TEM image of aggregated 5 nm citrate NPs in NaCl solution.

The high electron density of gold NPs provides an enormous scattering contrast compared to PEG and HSA; therefore, in SAXS experimental patterns, the direct contribution of PEG is neglected. The protein contribution for 40 nm NPs is considered in the sample with 4 mg mL^{-1} protein and for 5 nm NPs in samples with Pr/NP = 1000 and 4 mg mL^{-1} of protein.

In the experimental SAXS patterns, the upturn in the low q-range ($q < 0.1$ nm^{-1} for 40 nm NPs, and $q < 0.4$ nm^{-1} for 5 nm NPs) indicates the attractive interactions among the particles (aggregation).

3.1. Citrate-Capped Nanoparticles

Figure 1 shows the experimental SAXS patterns and the corresponding model-based fits for citrate-capped NPs in different environmental conditions. The SAXS patterns for samples with high colloidal stability, which are not aggregated, show a plateau in the low q-range. Stable NPs samples SAXS patterns are approximated using a form factor, $P(q)$, of polydisperse spherical particles model with the Gaussian size distribution on the NPs radius (see Equations (1)—(3)) using the SASfit[22] software.

In contrast, the aggregated samples with lower colloidal stability show an increase in forward-scattering (low q-range). To fit the SAXS curves of aggregated NPs samples, besides the form factor, the sticky-hard sphere model is considered as structure factor, $S(q)$ (see Equations (3)—(7)). The "stickiness", τ, is a parameter in this model that describes the strength of the attractive forces, and from Equations (3)—(7), it is clear that smaller τ means stronger attraction forces between NPs. In addition to this, since the SAXS resolution in our experimental setup is 210 nm, for larger aggregated NPs with radius beyond the resolution limit, a simple power-law is added similar to the Porod scattering of big particles to account for the low-q upturn (see Equation (8)).[27] All the fitting parameters are available in detail in the supporting information (Tables S1–S4, Supporting Information).

The citrate-capped sample with 40 nm in diameter, 40 nm citrate, in DI water does not show aggregation and data is fitted only with the form factor model for polydisperse spherical particles. The X-ray scattering length density difference between gold NPs and water, 1.13×10^{12} cm^{-2},[22] is considered as the constant parameter in all fittings since there is no change during the experiments and the mean radius parameter in the Gaussian size distribution model is selected to vary to have the best fit. Based on the final fit parameters, the mean radius is obtained with 18.7 ± 0.1 nm. The DLS measurement for this sample results in $d_h = 42.9 \pm 0.1$ nm with a polydispersity index (PDI) = 0.11 (Figure S3, Supporting Information), and is in a good agreement with our finding from SAXS data fitting.

In contrast, the citrate-capped sample with 5 nm in diameter in DI water shows aggregation; therefore, the sticky-hard sphere model, besides the form factor, is considered as the structure factor in the fitting equation. As discussed above, the mean radius parameter in the Gaussian size distribution model

is selected to vary and is obtained with 2.6 ± 0.1 nm. The stickiness parameter in the structure factor is selected to vary for a better fitting, and is 0.117 ± 0.001. The DLS measurement gives $r_h = d_h/2$ = 4.5 ± 0.1 nm with a PDI = 0.39 (Figure S3, Supporting Information). The r_h, 4.1 ± 0.1 nm, in comparison with the mean radius from the SAXS analysis, 2.6 ± 0.1 nm, shows the sensitivity and precision of the SAXS method in characterizing small gold NPs, specifically in low concentrations.

Both sizes of the citrate-capped NPs samples in NaCl solution show a considerable upturn in the low *q*-range of the scattering pattern; the samples exhibit precipitation, and black clots appear in the solutions.

In the SAXS data analysis, the sphere model as form factor and the sticky-hard sphere model as structure factor are considered, and a simple power-law is added to the background. In the structure factor model, for the 40 nm citrate NPs in NaCl solution, the stickiness parameter is 0.0973 ± 0.0002, which shows strong attractive forces. For the 5 nm citrate NPs sample, this parameter decreases from 0.117 ± 0.001 in DI water to 0.0862 ± 0.0001 in NaCl solution, indicating stronger attraction between NPs in NaCl solution.

In the cryo-TEM images, NPs coalescence is observed when 5 nm citrate NPs are placed in NaCl solution (Figure 1c), indicating a porous network structure.[28] The formation of such aggregates under cryogenic conditions confirms the visual observations and the results of our SAXS study.

In DLS measurements (Figure S3, Supporting Information) for 40 nm citrate NPs, the d_h in DI water, 42.9 ± 0.1 nm, increases enormously to 333.9 ± 0.1 nm in NaCl solution, and for 5 nm citrate from 8.1 ± 0.1 nm in DI water to 426.8 ± 0.1 nm in NaCl solution, showing the immense aggregation. This significant aggregation is related to higher IS in the NaCl solution compared to DI water. As discussed before, higher IS screens the NPs surface charge and, based on the DLVO theory, decreases the electrostatic repulsion between the NPs. Zeta potential and d_h measurements support these findings. Figure S3a,b (Supporting Information), shows the DLS autocorrelation function and size distribution by intensity for 40 and 5 nm citrate-capped NPs in DI water and NaCl solution. From the Stokes–Einstein equation, larger particles diffuse slower than smaller particles, and the related correlation function decays slower.[29] For both sizes of NPs, the correlation coefficient take a longer time to decay in NaCl solution compared to DI water, indicating the presence of larger particles in the sample and aggregation. Figure S3c (Supporting Information), shows the initial NPs mean zeta potential in DI water and its increment when NPs mix with NaCl solution. **Table 2** shows the DLS results for NPs samples in DI water and NaCl solution. For NPs samples in protein solutions, DLS measurements are not conducted as the NPs and protein signals cannot be differentiated.[30]

Another method to investigate the colloidal stability of gold NPs is UV–visible spectroscopy. For gold NPs, the SPR wavelength is around 520 nm and depends on the NPs size. The absorbance peak position directly relates to the NPs size. Respectively, redshift and blueshift of the absorbance peak position explain the changes to larger and smaller NPs sizes. In addition, peak broadening indicates the increase in the NPs polydispersity, proofing less colloidal stability.[31]

As **Figure 2** shows, for both sizes of citrate-capped NPs after mixing with NaCl solution, the resonance peak moves to higher wavelengths (redshift) and gets broader, indicating the aggregation.

Mixing citrate-capped NPs with NaCl solution containing HSA particles results in different behavior for 5 and 40 nm NPs. The minimum number of HSA particles covering the NPs surface entirely at a so-called "equilibrium" condition,[32] that is, after a particular time incubation of NPs with proteins, can be calculated from the division of the surface area of an individual NP by the contact area of one HSA particle. Here, the HSA particle is considered as a triangular prism and assumed to bind in a face-on configuration to the NP surface. Its contact surface is about 32 nm^2. This approach is widely used; however, it could underestimate the number of adsorbed proteins.[32,33] According to this method, and disregarding the NPs size distribution, for 5 nm NPs, 3, and for 40 nm NPs, 157 HSA protein particles are needed for a full coverage at equilibrium state.

40 nm citrate NPs, after mixing with NaCl solution containing 100 or 1000 protein per NP (Pr/NP ratio), aggregate and mostly precipitate immediately. The significant upturn in the SAXS patterns at low *q*-range (Figure 1a) confirms the aggregation. However, for the NaCl solution containing 4 mg mL^{-1} HSA providing a significant excess of proteins with a ratio Pr/NP >700 000, the SAXS pattern shows a plateau with no enhancement in the forward scattering. This means that most of the NPs are covered by proteins and stable.

In solutions with Pr/NP ratios of 1000, based on our theoretical consideration discussed above, enough protein particles are available to cover the NPs surfaces entirely. Nevertheless, since the IS of the NPs colloid is changing by NaCl, while the protein is added, due to strong electrostatic attractive forces after NPs charge screening, the probability of NP-NP interactions is much higher than NP-Pr interactions, which results finally in NPs aggregation. However, in the solution with a large excess of protein particles (Pr/NP >700 000), the

Table 2. DLS results for NPs samples in DI water and NaCl solution.

Samples	d_h in DI water [nm]	Polydispersity index [PDI]	Zeta potential in DI water ± SD (mV)	d_h in NaCl [nm]	Polydispersity index [PDI]	Zeta potential in NaCl ± SD [mV]
40 nm PEG	64.4 ± 0.1	0.09	−44 ± 1	65.1 ± 0.1	0.11	−3 ± 1
40 nm citrate	42.9 ± 0.1	0.11	−53 ± 1	333.9 ± 0.1	0.25	−30 ± 1
5 nm PEG	21.5 ± 0.1	0.32	−27 ± 4	23.1 ± 0.1	0.42	−15 ± 3
5 nm citrate	8.1 ± 0.1	0.39	−34 ± 2	426.8 ± 0.1	0.23	−22 ± 1

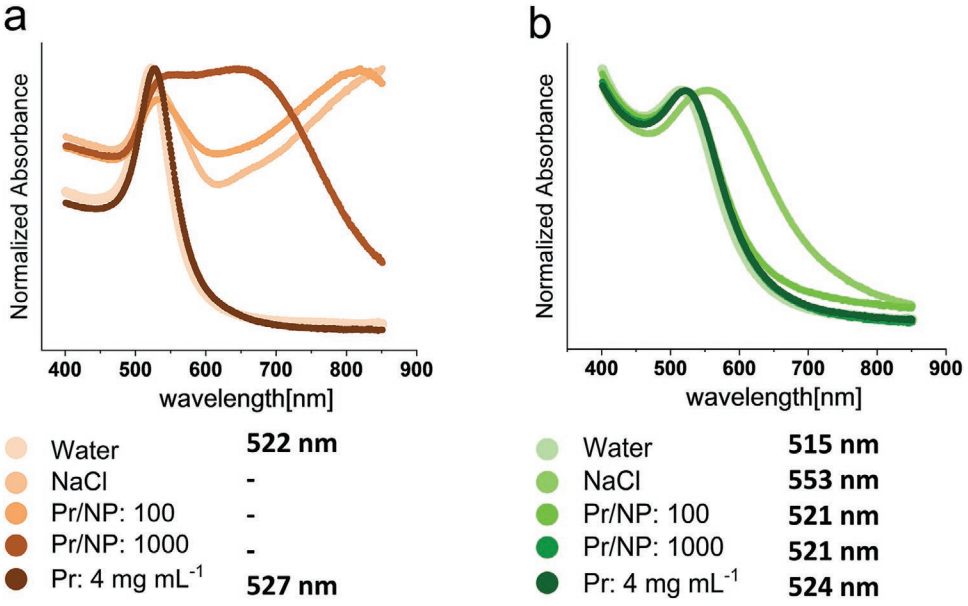

Figure 2. UV–visible spectra for citrate-capped NPs in different environments: a) 40 nm citrate, b) 5 nm citrate.

NP-Protein interactions are favored due to the very high protein concentration and can overcome the NP-NP interactions; consequently, the PC forms that stabilizes the NPs in the solution. Figure 1a,b shows the capillaries containing the NPs colloids in NaCl and protein solutions. The pink color indicates stable NPs or minor aggregation, and the colorless solutions show aggregated and precipitated samples. For the 40 nm citrate samples, only the capillary with the highest HSA concentration (4 mg mL^{-1}) shows the pink color indicating a stable NPs colloid.

In the SAXS data fitting for the gold NPs samples in the presence of protein, the same polydisperse spherical model with Gaussian size distribution is considered as form factor, the sticky-hard sphere model as structure factor, and power-law scattering is added. In addition, for 5 nm NPs samples in media containing Pr/NP = 1000, or 4 mg mL^{-1} protein and for 40 nm NPs in media containing 4 mg mL^{-1} protein, another contribution, a polydisperse spherical model with Gaussian size distribution, is considered as a form factor for protein particles. The X-ray scattering length density difference between protein and water is 2.25×10^{10} cm^{-2} [34] and is considered as constant parameter in the fitting procedure.

Therefore, the final intensity equation in the fitting process for citrate-capped NPs samples containing protein is:

$$I_{\text{total}}(q) = \left[P(q)S(q)\right]_{\text{aggregated gold NPs}} + \left[P(q)\right]_{\text{protein}} + \text{background power law term} \quad (11)$$

As already referred, the stickiness parameter in structure factor for the 40 nm citrate sample in NaCl solution is 0.0973 ± 0.0002 that by adding protein to the sample increases to 0.1002 ± 0.0002 and 0.1055 ± 0.0002 for Pr/NP = 100, 1000, respectively. This increment signifies weaker attractive forces between the NPs due to the protein binding; however, the NPs are aggregated and participated. Finally, for 4 mg mL^{-1} protein, no structure factor is needed in fitting since the particles stabilizes ultimately.

For 5 nm citrate NPs, the colloidal stability significantly increases after mixing with NaCl solution containing HSA. The SAXS pattern upturn in the low q-range for NaCl solution changes to a plateau, as shown in Figure 1b. The pink color of the capillaries in Figure 1b directly displays the NPs colloidal stability in protein solutions.

The stickiness parameter in the structure factor increases from 0.0862 ± 0.0001 in NaCl solution to 0.1128 ± 0.0001 at Pr/NP = 100, to the environment revealing the less strong attractive forces between NPs. By adding more protein to the system, this parameter decreases to 0.0973 ± 0.0002 and 0.0897 ± 0.0005 for Pr/NP = 1000 and 4 mg mL^{-1} protein concentration, respectively. These changes indicate stronger attractive forces between NPs in the presence of higher number of proteins that result in NPs aggregation but no precipitation due to the PC around the NPs.

Studies are reporting that the presence of protein molecules in the NPs environment could have a reverse effect on NPs colloidal stability and cause NPs aggregation.[35] Several parameters have direct and indirect effects on NPs and proteins interactions, namely the protein concentration in the media. For the 5 nm citrate sample, the NPs stabilize in the presence of the protein compared to NaCl solution. Nevertheless, by increasing the Pr/NP ratio, the attractive forces between NPs get stronger, and finally, in the solution with 4 mg mL^{-1} protein (>1400 protein particles per NP), they start to aggregate again, as indicated by an upturn in SAXS pattern in the lower q-range. This behavior shows that a large excess of proteins in the environment after a complete coverage on the NPs surface can induce aggregation, as previously reported in other investigations.[36]

These results show the effect of NPs size and protein concentration on the colloidal behavior of NPs in a biological environment. Low protein concentration can stabilize NPs with a size similar to the protein particle size, while for bigger NPs, a higher excess of protein particles is needed for NPs stabilization.

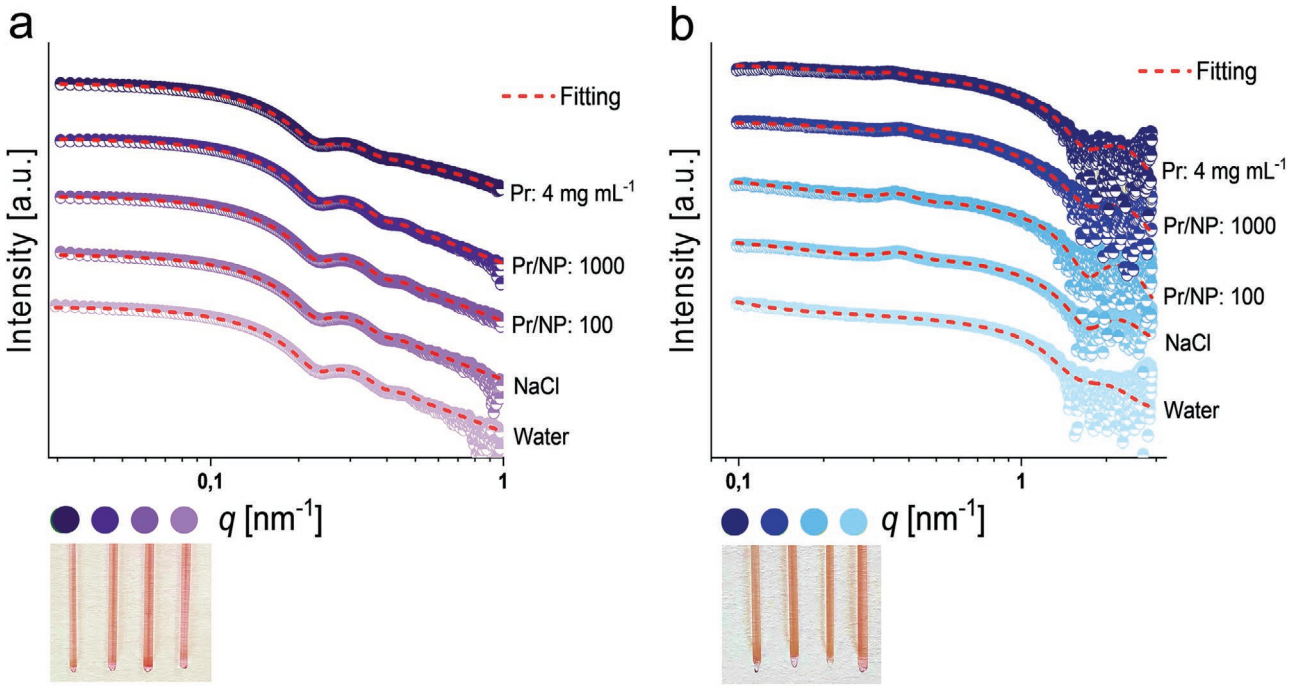

Figure 3. Experimental SAXS patterns and the corresponding model-based fits for PEGylated NPs in different environments: a) 40 nm PEG, b) 5 nm PEG. Below the graphs, the capillaries which were used in the experiments are shown. The pink color indicates stable gold NPs or NPs with minor aggregation.

The stabilization of citrate-capped NPs in NaCl solution containing protein particles with appropriate concentrations is also shown by the blueshift of the SPR peak in the UV–visible spectra, as shown in Figure 2. Both sizes of citrate-capped NPs in NaCl solution show tremendous aggregation, and by adding protein, NPs stabilize. However, in the case of 5 nm NPs, the excess protein can cause aggregation, which is shown by a slight increase in the SPR peak position.

3.2. PEGylated Nanoparticles

The 40 nm PEG sample shows the most stable NPs in DI water, NaCl solution, and media containing different protein concentrations. As it is shown in Table 2 and Figure S4a (Supporting Information), the d_h for this sample is 64.4 ± 0.1 nm in DI water with PDI = 0.09, and it changes to 65.1 ± 0.1 nm with PDI = 0.11 for NPs in NaCl solution that is not a notable change; however, the mean zeta potential (Figure S4c, Supporting Information) decreases in NaCl solution compare to DI water. High colloidal stability of samples with PEG surface modifications indicates that this polymer coating plays a notable role in gold NPs colloidal stability. The PEG brushes on NPs surfaces provide a steric stabilization and a short-range repulsive hydration layer around the NPs, creating excellent long-term stability in high IS and extreme pH.[37] In addition, PEG provides resistance to protein adsorption and is known as a biologically inert material.[38]

The d_h, for the PEGylated NPs is larger than their initial size measured by SAXS due to the strong hydration of the polymer brushes on the NPs surface. The PEG coating dramatically influences the NPs Brownian motion by introducing additional frictional drags, which reduce the NPs diffusivity. Accordingly, the correlation signal decays slowly in time, and the reported NPs sizes are larger.[29,30,39]

In **Figure 3**a, the experimental SAXS patterns and the corresponding model-based fits are shown. The SAXS patterns show a plateau in the low q-range. The same fitting strategies as for the citrate-capped NPs are used for PEGylated NPs. The mean radius parameter in the Gaussian size distribution model is selected to vary to have the best fit, and it is 18.7 ± 0.1 nm for 40 nm PEG sample in DI water, and it stays similar for NPs in other environments. By comparing this value with r_h = 32.2 ± 0.1, it is understood that the PEG shell in the presence of the gold core does not significantly contribute to the SAXS signal. However, for DLS measurements, their effect, together with their hydration, appears in d_h measurements.

In **Figure 4**, all SPR peak maxima occur at the same wavelength for the respective NPs samples in different media, demonstrating high colloidal stability. Compared to the citrate-capped samples, the SPR peak positions for the PEGylated samples are shifted by 2 nm, related to different dielectric constants of the NPs surrounding.

The PEGylate sample with 5 nm in diameter, 5 nm PEG, shows stability in DI water, and by applying the same model for the form factor, it is fitted with a mean radius of 2.6 ± 0.1 nm.

Surprisingly, the 5 nm PEG sample shows a unique behavior in NaCl solution (**Figure 5**a). In the SAXS pattern, we observe two peaks, the first is well distinct, and the second appears as a shoulder. By considering, $I(q) = P(q)S(q)$, the $S(q)$ can be calculated by dividing the experimental data by the one obtained from NPs in DI water as the form factor, $P(q)$. The two peaks (Figure 5b) are more evident in $S(q)$.

This information indicates the presence of 3D ordering of self-assembled particles. Several investigations for 2D and 3D

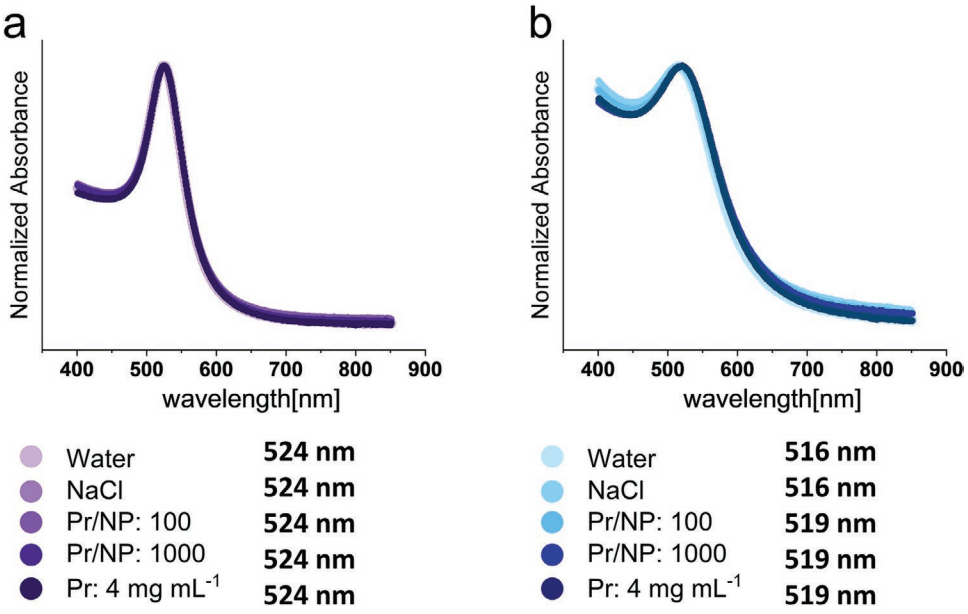

Figure 4. UV–visible spectra for PEGylated NPs in different environment: a) 40 nm PEG, b) 5 nm PEG. The redshift of absorbance peak shows a decrease in NPs colloidal stability.

self-assembling and crystallization of PEGylated gold NPs have been reported.[15b,40] These ordered structures are called superlattices[36] and possess novel physical properties compared to the individual NPs in solution due to the coupling between the NPs. Designing superlattices with controlled structures and suitable sizes is a significant challenge.[15b] One way is adding salt to stable PEG grafted gold NP colloids; the salt ions deplete into polymer brushes on the NP surface and generate an osmotic pressure gradient between the polymer shell and the salt solution. The self-assembly into the ordered crystal-like structure is ensured by partnering nearest neighbors to minimize the surface tension gradient at the interface between the polymer shell, and the high IS environment.[40e,41] The strategies for developing these superlattices are based on controlling NPs size, shape, volume fraction, kind and size of the functional groups on NP surfaces, the interparticle interactions, and the assembly environment.[40e]

It has been found that the ratio of the ligand chain size, L, to r, the NPs radius, $\chi = L/r$ has a significant influence on the final ordered superlattice structure. If this ratio is $\chi \leq 0.72$, the superlattice presents a face-centered cubic (FCC) structure, while a BCC structure is found for $\chi \geq 0.75$.[15b] In our system, the BCC structure is expected because the size of the PEG brush with 5 kDa molecular weight is 6 nm,[42] and $\chi = 6/2.5 = 2.4 \geq 0.75$.

To describe this BCC ordered structure, the two peaks in the SAXS pattern (Figure 5b) are fitted by a Gaussian peak function, giving a maxima at $q = 0.37 \pm 0.01$ nm^{-1} corresponding to a d-spacing = $2\pi/q = 17.0 \pm 0.1$ nm and at $q = 0.68 \pm 0.01$ nm^{-1} corresponding to a d-spacing = 9.2 ± 0.1 nm that are (011) and (112) reflections in the BCC structure, respectively.[15b]

The NPs are stable in the NaCl solution, and no precipitation is observed. The corresponding ordering (diffraction) peaks for the 3D-ordered BCC arrangement are not very pronounced in the SAXS patterns. Hence, the co-existence between the disordered NPs suspension and domains of ordered NPs is suggested. Only a part of NPs is localized in 3D-ordered domains but distributed in the entire sample volume.

In addition, besides the ordering (diffraction) peaks, the SAXS pattern shows an upturn in the low q-range, indicating NPs aggregation. Considering that SAXS data provide the average information of all particles and structures in the sample, the assumption for the co-existence of singlet NPs, aggregated NPs, and 3D-ordered NPs structures in the dispersion is valid.

To fit this data, as discussed above, we assume that there are attractive and repulsive forces available at the same time in the sample. Attractive forces result in aggregation and, in combination with repulsive forces, produce ordered domains. Therefore, for data fitting, two different contributions are considered.[27] One contribution includes the polydispersed spherical particles model as form factor and the BCC-iso-Gaussian (Figure S5, Supporting Information) model (see Equations (8)—(10)) as structure factor; the latter fits the ordering (diffraction) peaks perfectly. Another contribution includes the polydispersed spherical particles model as form factor and the sticky-hard sphere model as structure factor; the latter fits the upturn in the low q-range. Therefore, the final equation for fitting the SAXS curve of this sample is:

$$I_{\text{total}}(q) = \left[P(q)S(q)\right]_{\text{aggregated gold NPs}} + \left[P(q)S(q)\right]_{\text{ordered gold NPs}} + \text{background power law term} \quad (12)$$

This ordering behavior is not observed for the 40 nm PEG NPs samples which could be related to the low NPs or salt concentrations or the different PEG density on the NPs surface.

Based on the crystallographic analysis of the 5 nm PEG sample in NaCl solution, the size of the smallest ordered units, the unit cell, is derived with $a = 23.9 \pm 0.1$ nm[15b] for the BCC cell setting, which is in good agreement with the lattice constant = 22.9 ± 0.1 nm obtained from the SAXS data fitting.

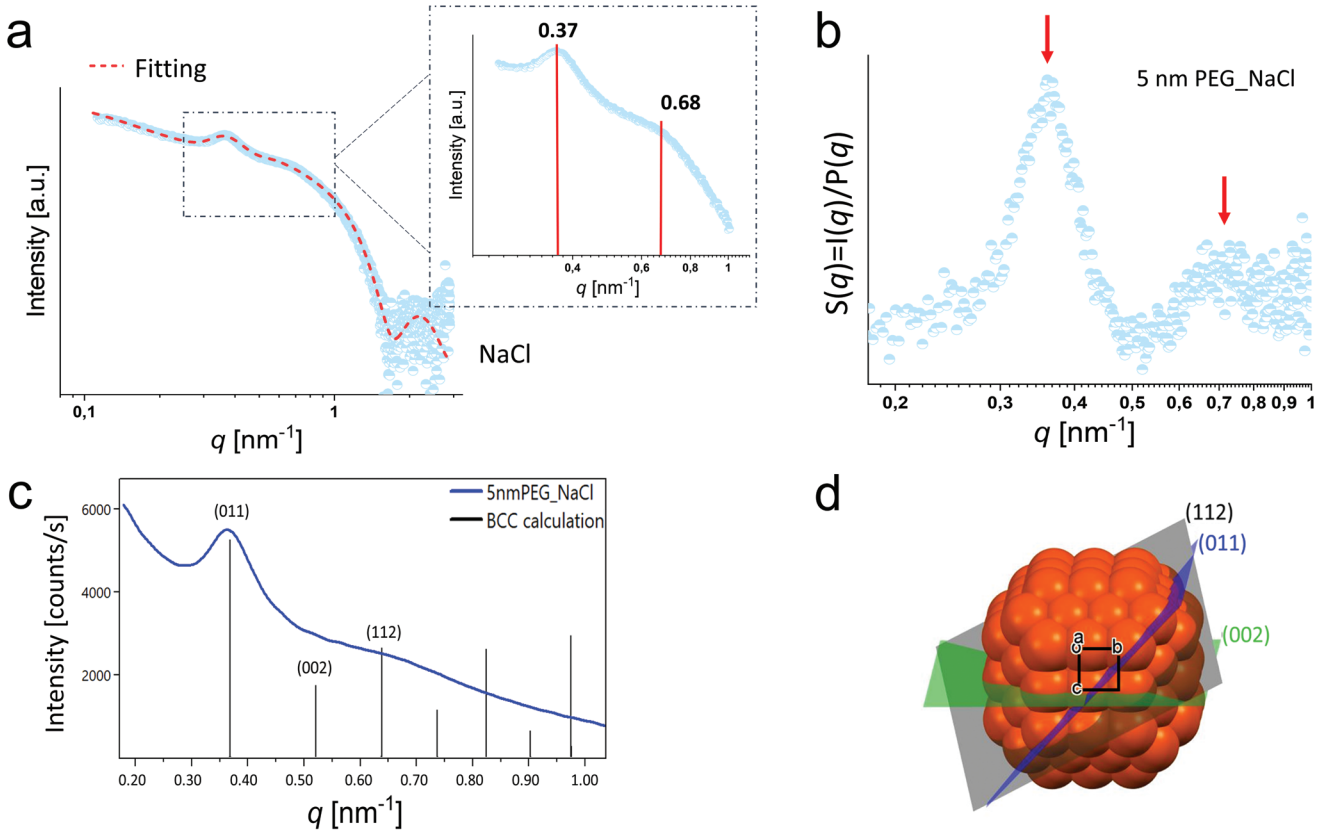

Figure 5. a) Experimental SAXS pattern for the 5 nm PEG sample in NaCl solution and corresponding co-fitting of the BCC structure model and the sticky-hard sphere model (details are available in supplementary information), b) Structure factor for 5 nm PEG sample in NaCl solution. c) Ordering (diffraction) peak indexing for the BCC structure for the 5 nm PEG sample in NaCl. d) Schematic view on the 3D NPs assembly visualizing the diffraction planes (011), (002), (112) of the applied BCC structural model.

An important parameter, which can be calculated through the assumption of the BCC structure, is the closest interparticle distance. The interparticle distance is the distance from one NP center to the nearest neighbor NP center (**Figure 6**). For the 5 nm PEG sample in NaCl solution, the interparticle distance in NaCl solution is 20.7 ± 0.1 nm and comparable with d_h = 21.5 ± 0.1 nm, measured by DLS (Figure S4b, Supporting Information).

The 5 nm PEG NPs system keeps its ordered structure even in the presence of proteins (Figure 3b). All data have been fitted using the same strategy as discussed above. For the samples with a ratio Pr/NP = 1000 and protein concentration of 4 mg mL^{-1}, a third contribution is considered in the scattering curve: a form factor for polydisperse spherical particles for protein particles.

The final equation for fitting these samples is:

$$I_{\text{total}}(q) = \left[P(q)S(q)\right]_{\text{aggregated gold NPs}} + \left[P(q)S(q)\right]_{\text{ordered gold NPs}} + \left[P(q)\right]_{\text{proteins}} + \text{background power law term} \quad (13)$$

Table 3 shows the first peak (011) information from the SAXS patterns for different protein concentrations.

The corresponding peak position in the SAXS patterns for the sample in NaCl solution moves from q = 0.37 nm^{-1},

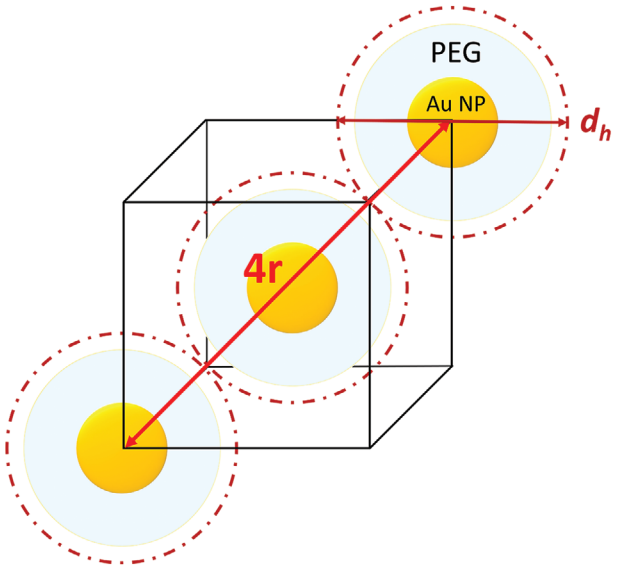

Figure 6. Scheme of 5 nm PEG NPs and their hydrodynamic radius, d_h, in a BCC structure. The interparticle distance (center-to-center distance) is calculated by $(\sqrt{3}a)/2$ and is comparable with the hydrodynamic diameter measured by DLS.

Table 3. 3D-assembly parameters obtained from ordering (diffraction) peak analysis and SAXS pattern fitting for 5 nm PEG NPs in different media.

Analysis type	(011) peak fitting and BCC calculations				SAXS pattern model-based fitting
Samples	Peak position q [nm^{-1}]	d-spacing [nm]	Interparticle distances [nm]	Lattice parameter a [nm] for BCC setting	Lattice parameter a [nm] for BCC setting
NaCl	0.37 ± 0.01	16.9 ± 0.1	20.7 ± 0.1	23.9 ± 0.1	22.9 ± 0.1
Pr/NP:100	0.36 ± 0.01	17.5 ± 0.1	21.5 ± 0.1	24.8 ± 0.1	23.4 ± 0.1
Pr/NP:1000	0.38 ± 0.01	16.5 ± 0.1	20.2 ± 0.1	23.3 ± 0.1	22.1 ± 0.1
Protein: 4 mg mL^{-1}	0.35 ± 0.01	17.9 ± 0.1	21.9 ± 0.1	25.3 ± 0.1	24.5 ± 0.1

d-spacing = 16.9 ± 0.1 nm, to a smaller q = 0.35 nm^{-1}, d-spacing = 17.9 ± 0.1 nm, for the solution containing 4 mg mL^{-1} protein. Accordingly, the BCC lattice constant obtained from SAXS data model-based fitting increases from a = 22.9 ± 0.1 nm to a = 24.5 ± 0.1 nm.

The lattice constants, d-spacings, and interparticle distances are slightly larger in the presence of HSA (Pr/NP ratio of 100 and large excess protein concentration of 4 mg mL^{-1}) compared to the sample with NaCl solution. This observation suggests that protein molecules penetrate inside the ordered 3D assembly of NPs and create a defect-like structure by replacing subsequently gold NPs. The similar size of gold NPs and protein molecules creates a competing environment that facilicates substitution of gold NPs by proteins in the periodic cubic BCC arrangement. An increasing protein concentration allows more protein molecules to penetrate the ordered structure (Table 3). The more flexible shape of the protein molecules compared to the relatively rigid shape of gold NPs could explain the enlargement of the 3D-ordered self-assembled structure with respect to the pure gold NPs arrangement.

The stickiness parameter for the 5 nm PEG NPs in NaCl solution and the samples containing protein is 0.1 suggesting no changes in the aggregation state of the NPs.

This ordering behavior is also confirmed by cryo-TEM. Cryo-TEM involves the vitrification of dispersions of NPs. Therefore, this approach allowed us to directly visualize and describe the aggregated states of NPs under different mixing conditions. Mixing 5 nm PEG NPs in NaCl solution led to extended self-assemblies (**Figure 7**a). The images show monolayers of NPs with a conserved distance of ≈16.5 nm extracted from the pair correlation calculation (Figure 7b). We could not confirm that the observed ordered 2D layers were in the solution or at the air-water interface; the cryo-TEM imaging technique captures only the positions of the NPs. However, based on previous findings by GI-SAXS,[40d] together with the tendency of particles to migrate to the air-water interface of the thin cryo-TEM samples,[43] we assume that the assembling could occur at the air-water interface. This compares to the interparticle distance of 20.7 ± 0.1 nm obtained from the SAXS pattern and the following crystallographic analysis for the ordered 3D arrangement. The smaller interparticle distance in the cryo-TEM method is most probably due to the NPs migration from the droplet volume to the air-water interface. It should be noted that in the blotting process, additional lateral forces might move the NPs more closely to each other and reduce the distances. PEGylated NPs tend to move to the air-water interface and get ordered. The monolayers of PEGylated NPs are also observed when back blotting is applied for the preparation of cryo-TEM samples or when a gold grid (Quantifoil company) is used. Several studies investigated this behavior.[40b,d]

Likewise, the NPs maintained the ordered assembly when dispersed in NaCl solution containing HSA. The interparticle distance extracted from the pair-distance correlation diagram increased to 19.5 nm, supporting the intercalation of HSA between the gold NPs in their respective environments

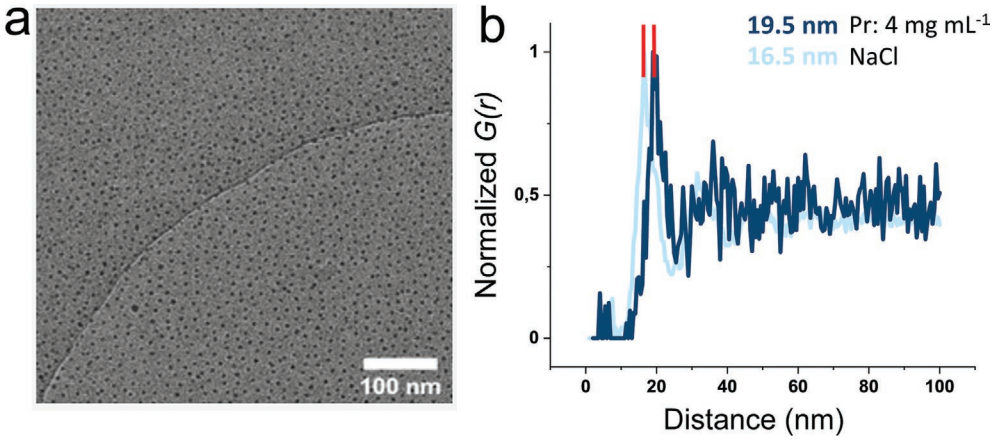

Figure 7. a) Cryo-TEM image of 5 nm PEG NPs in NaCl solution. Extended ordered assemblies of NPs are observed. b) Radial distribution function (RDF) from the cryogenic image of 5 nm PEG NPs in NaCl solution and protein solution with 4 mg mL^{-1} HSA, respectively. RDF calculation is performed on the positions of the monolayer of gold particles extracted from the tomogram.

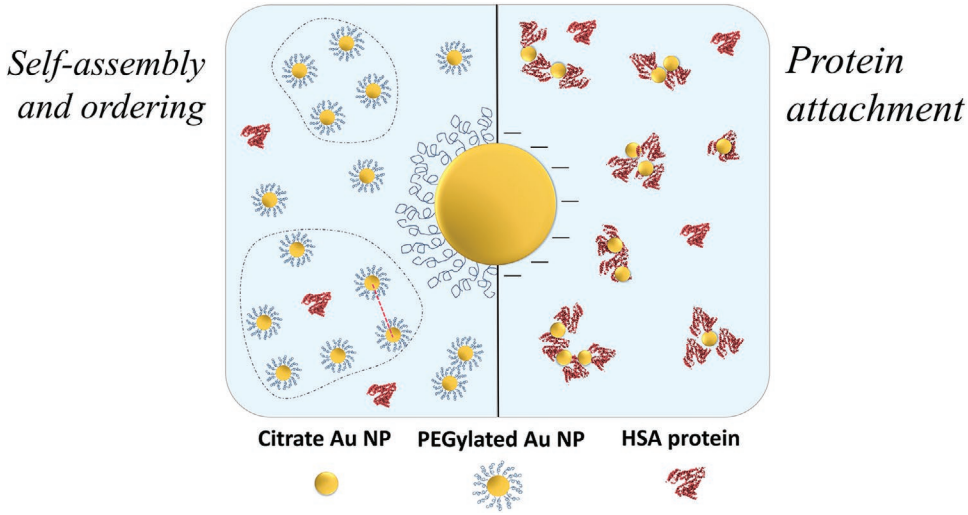

Figure 8. Two different stabilization mechanisms for gold NPs in biological environments containing HSA.

(Figure 7b). The shift of the interparticle distance to a higher value substantiated the finding by SAXS.

4. Conclusions

This study investigates the effects of NPs size, NP surface modification, and protein concentration on gold NPs colloidal stability. In-situ SAXS is a non-destructive technique enabling to study different NPs systems in their initial media, excluding any system perturbation through sample preparation. This is an advantage in biological studies, as it allows mimicking the biological environment as close as possible to the that found in the human body. The chosen model system of gold NPs in the HSA protein environment allowed us to study the influence of NPs size and surface modifications in different IS and protein concentrations. Interestingly, different mechanisms of NP colloidal stabilization with HSA protein have been identified and characterized in detail. 5 nm NPs with two different surface modifications, such as methoxy polyethylene glycol sulfhydryl (PEG) and citrate, exhibit two different pathways of NPs stabilization, as it is shown in **Figure 8**.

For PEGylated NPs, a stable 3D self-assembled ordered structure revealing an interparticle distance of 20.7 ± 0.1 nm in higher IS is observed. The NPs keep their ordering even in solutions with the highest protein concentrations of 4 mg mL^{-1}. However, the corresponding distance increases to 21.9 ± 0.1 nm related to the penetration of protein particles inside the ordered 3D structure. After adding the protein, this distance increment also is observed with cryo-TEM; however, the distances are smaller in cryo-TEM, most probably influenced by the sample preparation. The presence of two ordering (diffraction) peaks in the SAXS pattern suggests a BCC arrangement built up from gold NPs in an ionic environment for the ordered self-assemblies. The similar size of NPs and protein molecules creates a competing environment: increasing the protein concentration results in substituting gold NPs by proteins in the ordered NPs arrangement. The more flexible shape of the protein compared to the relatively rigid shape of gold NPs could explain the enlargement of the 3D-ordered arrangement compared to the pure gold NPs ordering.

For the 40 nm PEG sample, the PEG surface coating stabilizes the NPs perfectly in higher IS and protein solutions with different concentrations. However, for this system, no ordering behavior is observed.

Colloidal stability for citrate-capped NPs in NaCl solution decreases drastically, and NPs precipitate immediately. For citrate-capped NPs in the presence of protein, a different particle stabilization mechanism is observed. The protein particles attach immediately to the NPs surface resulting in high colloidal stability with a random distribution of NPs. However, based on the NPs size, a different protein concentration is needed for providing the high colloidal stability.

NPs, bringing new opportunities and innovative applications in the biomedical domain, require a safe and efficient usage. The understanding of the NP-Protein system is the first step forward to steer NPs properties for biomedical applications. SAXS based analysis allows investigations under realistic physiological conditions and provides qualitative and quantitative information about complex NP-Protein interactions. This is essential to direct the design and synthesis towards more stable and biocompatible NPs for biomedical applications. Our study is an important step forward in understanding NPs systems in biological media and will be expanded to investigate NPs systems in more complex environments such as human blood.

Supporting Information

Supporting Information is available from the Wiley Online Library or from the author.

Acknowledgements

The authors are grateful to the Swiss National Science Foundation (Project No. 173012, NI and AN) (Grant number 200020_185062, FS and QO) for financial support. PW is part of the Materials Challenge NanoScreen which is co-funded by the Competence Centre for Materials Science and Technology (CCMX).

Open access funding provided by ETH-Bereich Forschungsanstalten.

Conflict of Interest

The authors declare no conflict of interest.

Data Availability Statement

Research data can be made available from the authors upon request.

Keywords

aggregation, colloidal stability, gold nanoparticles, human serum albumin, protein corona, small-angle X-ray scattering, UV–visible spectroscopy

Received: October 10, 2021
Published online:

[1] T. L. Moore, L. Rodriguez-Lorenzo, V. Hirsch, S. Balog, D. Urban, C. Jud, B. Rothen-Rutishauser, M. Lattuada, A. Petri-Fink, *Chem. Soc. Rev.* **2015**, *44*, 6287.
[2] a) M. Kopp, S. Kollenda, M. Epple, *Acc. Chem. Res.* **2017**, *50*, 1383; b) L. Guerrini, R. A. Alvarez-Puebla, N. Pazos-Perez, *Materials (Basel)* **2018**, *11*, 1154; c) M. Suvarna, S. Dyawanapelly, B. Kansara, P. Dandekar, R. Jain, *ACS Appl. Nano Mater.* **2018**, *1*, 5524; d) A. Milosevic, D. Romeo, P. Wick, *Small* **2020**, *16*, 1907650.
[3] a) Â. Barreto, L. G. Luis, A. V. Girão, T. Trindade, A. M. V. M. Soares, M. Oliveira, *J. Nanoparticle Res.* **2015**, *17*, 1; b) S. Khan, A. Gupta, C. K. Nandi, *J. Phys. Chem. Lett.* **2013**, *4*, 3747.
[4] a) A. E. Nel, L. Madler, D. Velegol, T. Xia, E. M. Hoek, P. Somasundaran, F. Klaessig, V. Castranova, M. Thompson, *Nat. Mater.* **2009**, *8*, 543; b) T. Cedervall, I. Lynch, S. Lindman, T. Berggård, E. Thulin, H. Nilsson, K. A. Dawson, S. Linse, *Proc. Natl. Acad. Sci. U. S. A.* **2007**, *104*, 2050.
[5] N. I. Anaraki, A. Sadeghpour, K. Iranshahi, C. Toncelli, U. Cendrowska, F. Stellacci, A. Dommann, P. Wick, A. Neels, *Nano Res.* **2020**, *13*, 2847.
[6] a) N. R. Panyala, E. M. Peña-Méndez, J. Havel, *J. Appl. Biomed.* **2009**, *7*, 75; b) D. A. Giljohann, D. S. Seferos, W. L. Daniel, M. D. Massich, P. C. Patel, C. A. Mirkin, *Angew. Chem. Int. Ed. Engl.* **2010**, *49*, 3280.
[7] J. Polte, *CrystEngComm* **2015**, *17*, 6809.
[8] H. Neurath, H. B. Bull, *Chem. Rev.* **1938**, *23*, 391.
[9] S. L. Hirsh, D. R. McKenzie, N. J. Nosworthy, J. A. Denman, O. U. Sezerman, M. M. M. Bilek, *Colloids Surf., B* **2013**, *103*, 395.
[10] S. Angioletti-Uberti, M. Ballauff, J. Dzubiella, *Mol. Phys.* **2018**, *116*, 3154.
[11] a) M. Mahmoudi, I. Lynch, M. R. Ejtehadi, M. P. Monopoli, F. B. Bombelli, S. Laurent, *Chem. Rev.* **2011**, *111*, 5610; b) M. P. Monopoli, C. Åberg, A. Salvati, K. A. Dawson, *Nat. Nanotechnol.* **2012**, *7*, 779.
[12] C. Carrillo-Carrion, M. Carril, W. J. Parak, *Curr. Opin. Biotechnol.* **2017**, *46*, 106.
[13] C. Sanchez-Cano, R. A. Alvarez-Puebla, J. M. Abendroth, T. Beck, R. Blick, Y. Cao, F. Caruso, I. Chakraborty, H. N. Chapman, C. Chen, B. E. Cohen, A. L. C. Conceição, D. P. Cormode, D. Cui, K. A. Dawson, G. Falkenberg, C. Fan, N. Feliu, M. Gao, E. Gargioni, C.-C. Glüer, F. Grüner, M. Hassan, Y. Hu, Y. Huang, S. Huber, N. Huse, Y. Kang, A. Khademhosseini, T. F. Keller, et al., *ACS Nano* **2021**, *15*, 3754.
[14] a) T. Li, A. J. Senesi, B. Lee, *Chem. Rev.* **2016**, *116*, 11128; b) C. Sanchez-Cano, R. A. Alvarez-Puebla, J. M. Abendroth, T. Beck, R. Blick, Y. Cao, F. Caruso, I. Chakraborty, H. N. Chapman, C. Chen, B. E. Cohen, A. L. C. Conceicao, D. P. Cormode, D. Cui, K. A. Dawson, G. Falkenberg, C. Fan, N. Feliu, M. Gao, E. Gargioni, C. C. Gluer, F. Gruner, M. Hassan, Y. Hu, Y. Huang, S. Huber, N. Huse, Y. Kang, A. Khademhosseini, T. F. Keller, et al., *ACS Nano* **2021**, *15*, 3754.
[15] a) B. Abecassis, F. Testard, O. Spalla, *Phys. Rev. Lett.* **2008**, *100*, 115504; b) J. Schmitt, S. Hajiw, A. Lecchi, J. Degrouard, A. Salonen, M. Imperor-Clerc, B. Pansu, *J. Phys. Chem. B* **2016**, *120*, 5759.
[16] F. Spinozzi, G. Ceccone, P. Moretti, G. Campanella, C. Ferrero, S. Combet, I. Ojea-Jimenez, P. Ghigna, *Langmuir* **2017**, *33*, 2248.
[17] C. Moya, R. Escudero, D. C. Malaspina, M. de la Mata, J. Hernández-Saz, J. Faraudo, A. Roig, *ACS Appl. Bio Mater.* **2019**, *2*, 3084.
[18] R. E. Wang, L. Tian, Y.-H. Chang, *J. Pharm. Biomed. Anal.* **2012**, *63*, 165.
[19] N. Hondow, R. Brydson, P. Wang, M. D. Holton, M. R. Brown, P. Rees, H. D. Summers, A. Brown, *J. Nanoparticle Res.* **2012**, *14*, 977.
[20] C. E. Blanchet, A. Spilotros, F. Schwemmer, M. A. Graewert, A. Kikhney, C. M. Jeffries, D. Franke, D. Mark, R. Zengerle, F. Cipriani, S. Fiedler, M. Roessle, D. I. Svergun, *J. Appl. Crystallogr.* **2015**, *48*, 431.
[21] D. Franke, A. G. Kikhney, D. I. Svergun, *Nucl. Instrum. Methods Phys. Res., Sect. A* **2012**, *689*, 52.
[22] I. Bressler, J. Kohlbrecher, A. F. Thunemann, *J. Appl. Crystallogr.* **2015**, *48*, 1587.
[23] T. Degen, M. Sadki, E. Bron, U. König, G. Nénert, *Powder Diffr.* **2014**, *29*, S13.
[24] C. F. Macrae, I. Sovago, S. J. Cottrell, P. T. A. Galek, P. McCabe, E. Pidcock, M. Platings, G. P. Shields, J. S. Stevens, M. Towler, P. A. Wood, *J. Appl. Crystallogr.* **2020**, *53*, 226.
[25] W. Haiss, N. T. K. Thanh, J. Aveyard, D. G. Fernig, *Anal. Chem.* **2007**, *79*, 4215.
[26] a) L. G. Schulz, F. R. Tangherlini, *J. Opt. Soc. Am.* **1954**, *44*, 362; b) L. G. Schulz, *J. Opt. Soc. Am.* **1954**, *44*, 357.
[27] C. Pigliacelli, D. Maiolo, Nonappa, J. S. Haataja , H. Amenitsch, C. Michelet, P. Sánchez Moreno, I. Tirotta, P. Metrangolo, F. Baldelli Bombelli, *Angew. Chem., Int. Ed.* **2017**, *56*, 16186.
[28] M. Robins, A. Fillery-Travis, *J. Chem. Technol. Biotechnol.* **1992**, *54*, 201.
[29] A. P. Ramos, in *Nanocharacterization Techniques* (Eds: A. L. Da Róz, M. Ferreira, F. deLima Leite, O. N. Oliveira), William Andrew Publishing, New York **2017**, p. 99.
[30] N. I. Anaraki, A. Sadeghpour, K. Iranshahi, C. Toncelli, U. Cendrowska, F. Stellacci, A. Dommann, P. Wick, A. Neels, *Nano Res.* **2020**,*13*, 2847.
[31] a) V. Amendola, R. Pilot, M. Frasconi, O. M. Maragò, M. A. Iatì, *J. Phys. Condens. Matter* **2017**, *29*, 203002; b) X. Huang, M. A. El-Sayed, *J. Adv. Res.* **2010**, *1*, 13.
[32] J. S. Gebauer, M. Malissek, S. Simon, S. K. Knauer, M. Maskos, R. H. Stauber, W. Peukert, L. Treuel, *Langmuir* **2012**, *28*, 9673.
[33] L. Treuel, M. Malissek, S. Grass, J. Diendorf, D. Mahl, W. Meyer-Zaika, M. Epple, *J. Nanoparticle Res.* **2012**, *14*, 1102.
[34] J. C. Ang, M. J. Henderson, R. A. Campbell, J.-M. Lin, P. N. Yaron, A. Nelson, T. Faunce, J. W. White, *Phys. Chem. Chem. Phys.* **2014**, *16*, 10157.
[35] H. Wang, Y. Lin, K. Nienhaus, G. U. Nienhaus, *WIREs Nanomed. Nanobiotechnol.* **2018**, *10*, e1500.
[36] K. J. Si, Y. Chen, Q. Shi, W. Cheng, *Adv. Sci. (Weinh)* **2018**, *5*, 1700179.
[37] J. Schubert, M. Chanana, *Curr. Med. Chem.* **2018**, *25*, 4553.
[38] S. Lowe, N. M. O'Brien-Simpson, L. A. Connal, *Polym. Chem.* **2015**, *6*, 198.
[39] a) K. Rahme, L. Chen, R. G. Hobbs, M. A. Morris, C. O'Driscoll, J. D. Holmes, *RSC Adv.* **2013**, *3*, 6085; b) A. J. Chancellor, B. T. Seymour, B. Zhao, *Anal. Chem.* **2019**, *91*, 6391.

[40] a) A. A. Volkert, V. Subramaniam, M. R. Ivanov, A. M. Goodman, A. J. Haes, *ACS Nano* **2011**, *5*, 4570; b) W. Wang, H. J. Kim, W. Bu, S. Mallapragada, D. Vaknin, *Langmuir* **2020**, *36*, 311; c) H. Zhang, W. Wang, S. Mallapragada, A. Travesset, D. Vaknin, *J. Phys. Chem. C* **2017**, *121*, 15424; d) H. J. Kim, W. Wang, W. Bu, M. M. Hossen, A. Londono-Calderon, A. C. Hillier, T. Prozorov, S. Mallapragada, D. Vaknin, *Sci. Rep.* **2019**, *9*, 20349; e) H. Zhang, W. Wang, M. Akinc, S. Mallapragada, A. Travesset, D. Vaknin, *Nanoscale* **2017**, *9*, 8710.

[41] H. Zhang, W. Wang, S. Mallapragada, A. Travesset, D. Vaknin, *Nanoscale* **2017**, *9*, 164.

[42] a) J. V. Jokerst, T. Lobovkina, R. N. Zare, S. S. Gambhir, *Nanomedicine (Lond)* **2011**, *6*, 715; b) D. B. Chithrani, *J. Nanomed. Res.* **2014**, *1*, 00006.

[43] A. J. Noble, V. P. Dandey, H. Wei, J. Brasch, J. Chase, P. Acharya, Y. Z. Tan, Z. Zhang, L. Y. Kim, G. Scapin, M. Rapp, E. T. Eng, W. J. Rice, A. Cheng, C. J. Negro, L. Shapiro, P. D. Kwong, D. Jeruzalmi, A. des Georges, C. S. Potter, B. Carragher, *eLife* **2018**, *7*, e34257.